



LAWRENCE
LIVERMORE
NATIONAL
LABORATORY

Laser-based dynamic evaporation and surface shaping of fused silica with assist gases: a path to rimless laser machining

S. Elhadj, M. J. Matthews, G. M. Guss, I. L. Bass

August 16, 2012

Applied Physics B: Lasers and optics

Disclaimer

This document was prepared as an account of work sponsored by an agency of the United States government. Neither the United States government nor Lawrence Livermore National Security, LLC, nor any of their employees makes any warranty, expressed or implied, or assumes any legal liability or responsibility for the accuracy, completeness, or usefulness of any information, apparatus, product, or process disclosed, or represents that its use would not infringe privately owned rights. Reference herein to any specific commercial product, process, or service by trade name, trademark, manufacturer, or otherwise does not necessarily constitute or imply its endorsement, recommendation, or favoring by the United States government or Lawrence Livermore National Security, LLC. The views and opinions of authors expressed herein do not necessarily state or reflect those of the United States government or Lawrence Livermore National Security, LLC, and shall not be used for advertising or product endorsement purposes.

Laser-based dynamic evaporation and surface shaping of fused silica with assist gases: a path to rimless laser machining

S. Elhadj, M.J. Matthews, G.M. Guss, I.L. Bass

Lawrence Livermore National Laboratory, Livermore, California 94550, USA

email: elhadj2@llnl.gov

Abstract

Evaporation and ablation are fundamental processes which drive laser-based material processing performance. In applications where final surface shape is important, control of the temperature field and the resulting spatially-varying material response must also be considered. For that purpose, assist gases can prove useful in, first, lowering treatment temperatures and, second, in changing the interfacial and bulk chemistry to limit the capillary-driven flow conditions. Additionally, laser-matter coupling is strongly influenced by pulse length as it determines the heat affected. Using infrared imaging of CO₂ laser heated fused silica and surface profile measurements, we derive temperature and exposure time dependent pitting rates along with surface shapes across a range of gas conditions that include hydrogen, nitrogen, air, and helium. In the temperature range considered here (1500K to 4500K), evaporation, melting, flow, and densification are all shown to contribute to the final pit shape. Analysis reveals a strong and complex dependence of rim formation on both heating time and gas chemistry, mostly through a lowering of treatment temperature. Under dynamic hydrogen conditions, chemicapillarity appears to help in lowering rim height, in spite of the mass transport limitations of the reactants. A coupled heat and mass transport model that accounts for the relevant solid-gas phase chemistry is used to model the evaporation part of the pitting process. The data on this gas assisted approach suggests the possibility for sub-nanometer “rimless” laser-based machining.

1 Introduction

Fused silica is a critical optical component in high power lasers and will typically damage above a threshold fluence [1]. For stable and long term high power laser operation, the surface damage sites are mitigated by laser-based material removal leaving a pit on the order of a few 100 microns, which is precisely shaped to prevent beam modulation and damage re-initiation [2]. Careful control of surface shape and of the laser-induced temperature field remains important to reduce residual stress, redeposit formation, and beam focusing effects from minute surface profile alterations.

Enhancements in laser machining rates and shape control are possible with application of assist gases in place of machining under an ambient atmosphere. Such an approach is well-known in the field of laser welding and cutting, for instance laser cutting of metals in which assist gasses are used to physically disperse molten material [3]. Assist gases can also contribute to increased mass transport rates through higher diffusivities and convection, creation of alternative evaporative reaction pathways, and shifting of

the equilibrium point for the evaporation products. Previous studies under CW (seconds) laser heating conditions indicated that flow of a reducing gas such as hydrogen (H_2) increased evaporation rates manifolds [4] via a reduction reaction ($SiO_2 + H_2 \rightleftharpoons SiO + H_2O$) [5]. Even inert gases such as pure nitrogen (N_2) produced greater evaporation rates by pushing the reaction equilibrium forward. In contrast, the oxygen (O_2) in air, which is a product in the thermal decomposition reaction of silica, tends to inhibit evaporation ($SiO_2 \rightleftharpoons SiO + \frac{1}{2}O_2$) by the reverse silica condensation reaction. Mass transport limited kinetics in this regime of rapid evaporation near silica boiling point $\approx 3000K$ (BP) implies that laser-based evaporation is locally near equilibrium, where both forward and backward reactions can proceed to near completion [4]. Therefore, the temperature dependence of the equilibrium constants and free energy ΔG° ($K_p = \exp(-\Delta G^\circ/RT)$) become important in determining the extent of rate enhancements, and the degree to which a specific gas can be used to reduce treatment temperature, yet still allow sufficient evaporation rates for effective laser machining. Ideally, a gas is selected to produce the most volatile and stable evaporation products at a given temperature, which limits the thermal load on the treated sample.

Along with efficient material removal rates, the final shape of the laser machined pit is also important, particularly when considering laser processing of optical components in high power laser systems. Indeed, the lowering in laser treatment temperature through use of a dilute reducing gas can also lead to reduced rim formation at the periphery of the heated spots, producing an optically less caustic site [6]. Rim formation is driven by capillarity-related effects which can induce motion of the molten material at the free surface depending on the temperature dependence of the surface tension, σ and viscosity μ . A negative dependence, $d\sigma/dT < 0$, whether from compositional, thermal gradients, or interaction with a gas [7], induces an outward flow of material from the hot to the cold regions of the laser heated area, while a positive dependence reverses the flow direction [8]. The flow is kinetically limited by viscosity often represented with an Arrhenius relationship, $\mu(T) \propto \exp(E_a/RT)$ [9]. The dimensionless Marangoni number represents the balance of these forces for a thermal gradient ΔT over the size of the flowing melt pool, $M_a = d\sigma/dT \times (R_0 \Delta T / \mu \alpha)$, where R_0 is a characteristic length and α is the thermal diffusivity of silica, with buoyancy forces being negligible over the length scales considered here. Thus, a reduction in temperature should increase μ minimizing or, even, eliminating rim formation if the surface relaxation occurs over time scales much larger than the laser heating and thermal diffusion times.

Left unexplored in previous studies was the question of whether solid-gas phase reaction chemistry remains significant for non-equilibrium situations, when shorter pulses are used, and how short exposures affect rim formation. We present here measurements of pulse length dependent CO_2 laser evaporation studies in H_2 and in air, related rim height information; and contrast these results with CW steady laser heating for dilute H_2 , air, N_2 , and Helium (He) gases. Taken together, these gases represent reducing, oxidizing, neutral, and high diffusivity conditions, respectively. We extend our measurements to lower temperatures by $\approx 1000K$ from previous studies performed in the 2500K to 3000K range [4]. For this lower heating regime around 1500K, silica densification ($\approx 2-3\%$) from structural relaxation is dominant[10] but material flow is negligible due to the high viscosity of fused silica at those temperatures [9,11]. In contrast, with short and intense microsecond pulse exposures, temperatures

up to 4500K are reached, a regime where evaporation and melt flow dominate final surface shape. Differences in dynamic rim height formation from H₂ and air treatments are discussed, along with results of rim formation scaling with gas-assisted laser etch rate and temperature.

Our previously reported modeling efforts of laser-based evaporation kinetics used an empirical correlation function to describe the mass transfer coefficient, h_m , in the equation relating evaporation rates, R , with the equilibrium evaporation product concentration of silica $[\text{SiO}]_{\text{eq}}$, $R = h_m[\text{SiO}]_{\text{eq}}$ [4]. $[\text{SiO}]_{\text{eq}}(T)$ was experimentally derived from knowledge of the evaporation chemistry of SiO₂ in the presence and absence of H₂ reactant, and with knowledge of the related equilibrium constants. Here we compare experimental results with this model that includes coupled heat, mass, and reactive processes based on knowledge of the known temperature dependent evaporation chemistry, viscous properties, and laser-material coupling parameters.

2 Experimental

A schematic of the laser setup used to locally heat and apply gas to the surface of the fused silica sample is shown in Fig. 1(A). Figure 1(B) illustrates the heating, resulting surface pit, and mass transport processes for the experimental configuration. Temperature measurements were obtained from our infrared imaging system of the blackbody radiation emitted during heating, which was validated and described as reported elsewhere [12]. The amount of evaporated silica was estimated from the surface shape profiles obtained by interferometry measurements following laser treatment of the surface as described previously [4]. Finally, gas flow rate levels were adjusted with a mass flow controller (400-2000 sccm), directing a normal incidence gas jet towards the sample surface through a custom nozzle equipped with a laser window for simultaneous co-incident laser heating. In general, the evaporation rate was weakly but significantly dependent on gas flow in the range used in this study, varying by less than 5% for all gases used. Additional details of the measurements and setup are provided below.

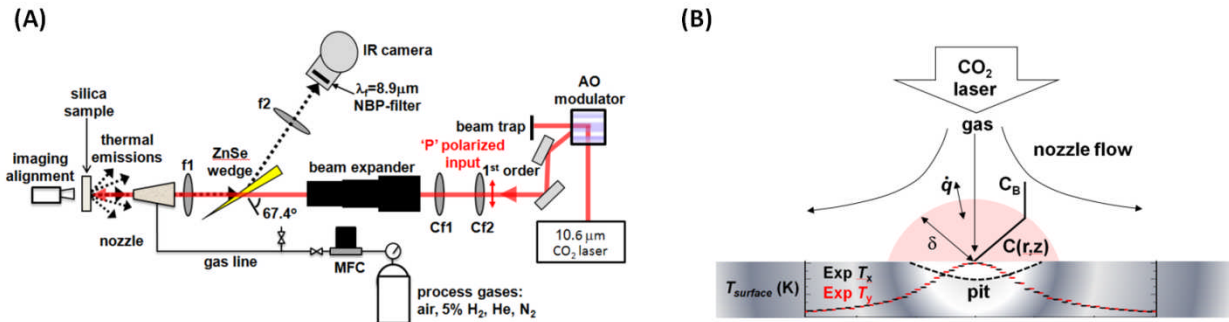


Fig. 1 (A) Schematic of the experimental setup used for evaporation of fused silica with CO₂ laser heating. A nozzle with a 3 mm opening and a mass flow controller (MFC) are used to bring an impinging gas coincidently with the laser beam at a controlled flow rate of the treatment gas from 400-2000 sccm. Lenses for beam focusing and magnification are indicated as f1, f2, cf1, cf2. (B) The laser-based evaporation produces a pit shape measured using white light interferometry *ex situ*. The surface depth profile is shown for the dashed line drawn through the center of the pit, along with the corresponding surface temperature profile, $T(K)$, captured *in situ* with the infrared camera imaging system. The reaction zone where species concentration varies is of size δ depending on fluid properties (ex. gas diffusivity), flow rate, flow

configuration, and the reactions within the zone and at the surface. Exchange with the bulk flow occurs at a rate $q \propto D/\delta$ which determines the materials laser driven evaporation rates.

2.1 Heating of silica surface

For near steady, long exposures, localized heating and evaporation of the silica surface was achieved with a focused CW ($\lambda_L = 10.6 \mu\text{m}$) CO₂ laser beam from a Synrad Firestar V20 (Synrad, Mukilteo, WA, USA), with a maximum output power of 20W and power stability of ~1% over the duration of the exposure. The laser beam profile was nearly a perfect Gaussian with a $1/e^2$ diameter of ~0.4 mm, as characterized by the knife edge method. The laser power delivered to the sample was set between 1.5 and 4.0W for the steady heating experiments with fixed exposures of 5 s. To study the effects of shorter pulses, another laser system with higher power and microsecond power control was utilized. It consists of a Synrad Firestar T100 RF excited CO₂ laser operating at 10 kHz and 50% duty cycle with a peak power of 110 W and an average power of 55 W and beam diameter of 100 μm ($1/e^2$) as characterized by a Photon Inc. Nanoscan beam profiler. The laser passes through an acousto-optic modulator to modulate the power reaching the silica surface. The modulator was driven with a square pulse with prescribed lengths ranging from 10 μs to 5 s and amplitudes ranging from 0.5 to 55 W average power. The ratio of the average power to pulse length was predetermined to yield an approximately 3 μm deep ablation pit. For pulse lengths above 100 μs , which is the period of the laser output, the silica was exposed to multiple cycles of the inherent power variation of the laser. In this regime the exposure is quasi-CW and the average power becomes relevant. For 10 and 50 μsec pulse lengths, the output was centered on the peak of one cycle of the power variation. In this regime the peak power is more relevant. For 10 μs pulse length the maximum power was not enough to create a 3 μm deep pit in one shot, so 6 successive shots were used.

2.2 Gas treatment of the silica surface

The samples used in this study were Corning 7980 (type III) fused silica (50 mm diameter, 10 mm thick discs). They were fixed vertically on a stage in ambient air and treated by injecting reactive gases using a nozzle with a 3 mm opening in front. Sample-surface spacing was kept fixed ~5 mm. The gas jet impinged normal to the surface plane and submerged the treated area well beyond the boundaries of the heated site by displacing the ambient air at the reacting surface before onset of laser heating. The laser beam passes through a transparent ZnSe window mounted on the backside of the nozzle and on to the surface through the nozzle front side opening. Compressed gas cylinders were used as the source for the following four dry gases (<1 ppmv H₂O), with trace amounts of impurities (< 3 ppmv): 1) dry air (78% nitrogen, 21% oxygen, 1% trace gases), 2) 100% nitrogen, 3) 5% hydrogen, 95% nitrogen, 4) 5% hydrogen, 95% helium. A calibrated OMEGA gas flow controller (FMA 3400) allowed setting the volumetric flow rate to levels around 1 sccm/min. The flow was started at least a minute before laser exposure to insure that all the dead volume was removed from the lines and that surface gas submersion was at steady state.

2.3 Depth profile measurement of the silica surface

As discussed elsewhere in details [4], the total depth of a pit created by laser heating at a given temperature and exposure length is a contribution from the amount of silica evaporated, the amount of melted silica displaced by flow, and the reduction in silica volume through densification. At temperatures approaching silica boiling point ($\approx 3000\text{K}$), pit depth is dominated by evaporation, while below the softening point of fused silica (1853K for Corning 7980), the depth is dominated by densification. To derive pitting and evaporation rates, the depths of the laser-induced pits were measured with a white light interferometer (Zygo Corp., Middlefield, CT, USA) to obtain a three dimensional image of the silica surface. The maximum depth was measured from the profile with $\approx 1\text{ nm}$ accuracy and lateral resolution of $\approx 0.5\text{ }\mu\text{m}$. Experimental depth ranged from 10 nm up to $40\text{ }\mu\text{m}$ depending on laser power, exposure time, and assist gas used for a particular site. Pitting rate was then calculated by taking the axial depth and dividing by the exposure time for the axial temperature measured.

2.4 Temperature measurement of silica surface

During laser exposure, the sample surface temperature was derived from *in situ* measurements of the blackbody emission of the heated spot using a calibrated LN-cooled HgCdTe camera operating at 33 fps and equipped with a $\lambda_p=8.9\text{ }\mu\text{m}$ narrowbandpass cold filter [12]. Although the optical resolution of the camera was $\sim 40\text{ }\mu\text{m}$ (sampled at $40\text{ }\mu\text{m}$ spacing), it can be shown that the calculated temperature profile established by a 0.4 mm beam varies slowly over the length scales studied here. Thermal imaging in a narrow band of the far infrared (λ_p) spectrum is crucial because it probes the surface emission emanating exclusively from within $\sim 1\text{ }\mu\text{m}$ of the outer surface of silica, which results in an accurate temperature measurement of the interface rather than a bulk average over a gradient [13]. For further details, the 2D surface temperature measurement method used in this study was validated and described elsewhere [12-14]. For short laser exposure experiments ($t_{\text{exp}} < 0.1\text{ sec}$) the IR camera frame rate was too slow, therefore the peak temperature was roughly estimated using the pit depth, d , and the known laser-based fused silica evaporation rates measured recently and correlated with the following equation, $A \exp[-E_{\text{evap}}/RT]$ [4,15], such that $T = (-E_{\text{evap}}/R)/\ln[(\rho d/At_{\text{exp}})]$, where ρ is silica density, $A = 6.25 \times 10^3\text{ }\mu\text{g}/\mu\text{m}^2/\text{sec}$, and $E_{\text{evap}} = 120.1\text{ kcal mole}^{-1}$. For these pulse lengths $< 100\text{ ms}$ the peak temperatures for both H_2 and air gases were nearly identical to within $\approx 5\text{K}$, ranging from 3250K up to 4525K for the shortest pulse of $10\text{ }\mu\text{sec}$.

3 Results and discussion

3.1 Evaporation kinetics for un-steady laser heating

The gas-solid reaction dynamics was assessed by measurement of the relative evaporation rates of silica in air and in $5\%\text{ H}_2/\text{N}_2$ ($R_{\text{H}_2}/R_{\text{AIR}}$) for laser exposures from $10\text{ }\mu\text{sec}$ up to 5 sec as shown in Fig. 2(A). H_2 reaction with silica is not apparent until the $\approx 100\text{ ms}$ exposure time is reached, at which point the relative rate rose continuously reaching a 3 fold increase for 5 sec exposures due to the added evaporation reaction of H_2 with SiO_2 . For these experiments, laser power levels were adjusted for each exposure such that approximately the same final depth was reached for each evaporation pit ($d = 2.75\text{ }\mu\text{m} \pm 0.25\text{ }\mu\text{m}$). In this manner, the amounts of material removed by evaporation were similar and rim

height differences more easily interpreted. The rate measurements are compared to a model based predictions described later, showing that an estimated ≈ 10 fold increase in evaporation rate is possible by using concentrated H_2 gas instead of 5% H_2 . Furthermore, the onset of the effect of H_2 is predicted to shift to shorter exposure times ≈ 10 ms. The lack of effect for short pulses is not surprising considering that the process is known to be mass transport limited as discussed earlier. A quick estimate of the H_2 feed flux based on bulk gas flow rate, H_2 concentration, and nozzle size gives a bulk transport rate of $\approx 1.9 \times 10^{-4} \mu\text{g}/\mu\text{m}^2\text{s}$. The diffusive flux over the beam heated area $R_0=0.4$ mm diameter and 5% molar bulk concentration, C_B , can be estimated from Fickian diffusion as $D_{H_2}C_B/R_0=1.0 \times 10^{-6} \mu\text{g}/\mu\text{m}^2\text{s}$ ($2.0 \times 10^{-5} \mu\text{g}/\mu\text{m}^2\text{s}$ for $C_B = 100\%$), with $D_{H_2} \approx 10^{-4} \text{m}^2/\text{sec}$. This limiting value can be compared to the typical experimental evaporation rates based on pit depth of $\approx 6.0 \times 10^{-5} \mu\text{g}/\mu\text{m}^2\text{s}$ for 100 ms exposure, and $\approx 6.0 \times 10^{-1} \mu\text{g}/\mu\text{m}^2\text{s}$ for a 10 μsec pulse, which clearly indicates that the thermal decomposition removal rate of silica from laser heating is 1 to 5 order of magnitude larger than the H_2 transport rate, hence the lack of apparent H_2 effect in Fig. 1(A). As these transport rates become comparable for longer exposures ($\approx 4.4 \times 10^{-6} \mu\text{g}/\mu\text{m}^2\text{s}$ for 5 sec exposure), the removal rates increase accordingly, and increase with C_B concentration as predicted by the model. Although the gas-etch dynamics described in Fig. 2(A) are specific to the laser spot size, temperatures, and gas concentration in this study, they reveal that the spontaneous decomposition of silica is much faster than the reactant transport for short pulse conditions, and will thus remain unaffected by gas chemistry even for highly reactive species until near steady heating conditions are reached.

3.2 Rim formation for un-steady laser heating

The question of whether shorter pulses could be used to reduce rim size, and whether solid-gas reactions can still play a role on these time scales was addressed next. Measurements of the rim height dependence on pulse length are shown in Fig. 1(B). The data reveals a complex but similar dependence for H_2 and air gases, although H_2 treated sites systematically produced smaller rims than those treated in air except for the lowest and highest exposures around 10 μsec and 1 sec, respectively. Notably, although H_2 has no apparent effect on evaporation rates in the range between 0.1 to 100 ms, it maintains a significant effect on rim height over that same range, indicating that *some* solid-gas reactions and interactions do take place at the surface, sufficient to produce smaller rims. Since the temperature profiles were nearly identical in both cases given the similarities in depths and laser parameters used, the differences suggest that chemicapillary driven flow must also play a role by opposing the outward thermocapillary force, such that the net results is a smaller driving force for the rim formation in H_2 , $|d\sigma/dT|_{H_2} < |d\sigma/dT|_{AIR}$. Reaction of hydrogen with silica is known to produce a hydroxylated surface by a so-called tarnishing process [16] involving diffusion-reaction of H_2 ($\text{SiO}_2(\text{s}) + \text{H}_2(\text{g}) \rightarrow \text{SiOH}(\text{s}) + \text{SiH}(\text{s})$). The surface tension is expected to be lowered by this tarnishing process for surfaces terminated with silanol (-OH) [17]. However, the OH spatial distribution during laser heating, interaction with the vapor phase, magnitude and sign of $d\sigma/dT_{H_2}$ remain uncertain [17]. Thus interpretation of the rim height differences is not straightforward. Furthermore, one must also assume that most of the flowing melt has not reacted with H_2 since OH in the silica network reduces viscosity by an order of magnitude over a few 100 ppm level changes [18], which would tend to facilitate flow and rim formation contrary to what was observed experimentally. In the case of H_2 gas application,

a lack of OH within the bulk is likely for the shortest pulse of 10 μsec for which the expected penetration depth of H_2 , $\sqrt{4t_{\text{exp}}D_{\text{bH}_2}} = 200 \text{ nm}$ with H_2 bulk diffusivity, $D_{\text{bH}_2} \approx 10^{-5} \text{ cm}^2 \text{ s}^{-1}$ [19], but for a 1 sec exposure the expected depth is 63 μm , reaching well beyond the melted zone and the assumption of OH free melt cannot hold. Thus the results with H_2 are counter intuitive, and more experimental work is needed to determine the fundamental properties of H_2 treated surfaces under these intense laser heating conditions.

The intricate pulse length behavior in Fig. 2(B) is also still not clear and is currently being addressed for future publication, along with the gas chemistry effect noted above. Briefly however, the dependence is likely related to the complex interplay between viscosity, heating rates and times, interfacial energies, and the peak temperatures applied. As the pulses get shorter, the laser power and temperature needed to produce the target pit depth also increase from 3000K up to 4500K. Viscosity and resistance to flow decrease exponential as a result, yet the effective time allowed for flow is reduced countering the effects of the lowered viscosity. The reversal in rim heights in Fig. 2(B) could reflect such antagonist tendencies. Likewise, for short pulses the depth of the heat affected zone, which scales with thermal diffusion and exposure time, would reduce the melted pool available to form a rim and the size of the rim, which is consistent with the lowering of the rim trend observed for the shortest pulses.

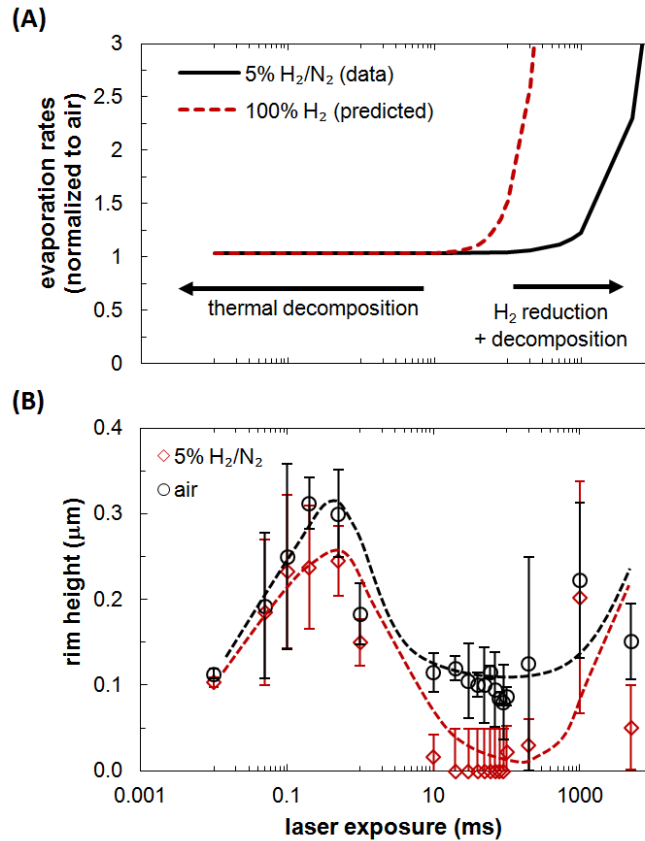


Fig. 2 (A) Relative evaporation rates ($R_{\text{H}_2}/R_{\text{Air}}$) dependence on pulse length in 5% H_2/N_2 gas and in air. The data is compared to the model predictions for 100% H_2 gas. (B) The corresponding rim heights

measurements are shown for the rims that form at the periphery of the laser-induced evaporation pits for the same conditions as in (A).

3.3 Evaporation kinetics and rim formation for steady laser heating

After focusing on dynamic pulse length effects, measurements of rim heights, pit profiles, and temperature were made for near steady heating conditions using a fixed exposure of 5 sec. For the beam parameter and experimental setup used, the surface temperature reaches a steady state after ≈ 1 sec of CW exposure [4,12,13]. In Fig. 3(A), a comparison of the pitting rates for 5% H_2/N_2 , 5% H_2/He , air, and 100% N_2 is shown. Air produced the largest rims for a given pitting rate, followed by 100% N_2 , 5% H_2/N_2 , and 5% H_2/He , in that order. This result is not surprising considering that greater evaporation rates are possible for a given temperature with reactive gases, such as H_2 , or for gases that shift the evaporation equilibrium forward, such as 100% N_2 . Helium with H_2 appears to have the added benefit of greater diffusivity that increases the transport and evaporation rates. Thus, for equal etching rate and exposure time, gases that promote silica evaporation will have done so at a lower temperature, producing smaller rims. The lower temperatures increase silica viscosity and reduce its ability to flow by capillarity, especially since the temperature dependence of the surface tension is much weaker than that of the viscosity. This results is illustrate in Fig. 3(B) showing a $\approx 200\text{K}$ reduction in treatment temperature by 5% H_2 to achieve the same depth as that in air, yet with a much lower rim size from the corresponding spatial profiles. Selection of an active etching gas therefore minimizes rim formation producing a more planar and less optically caustic surface.

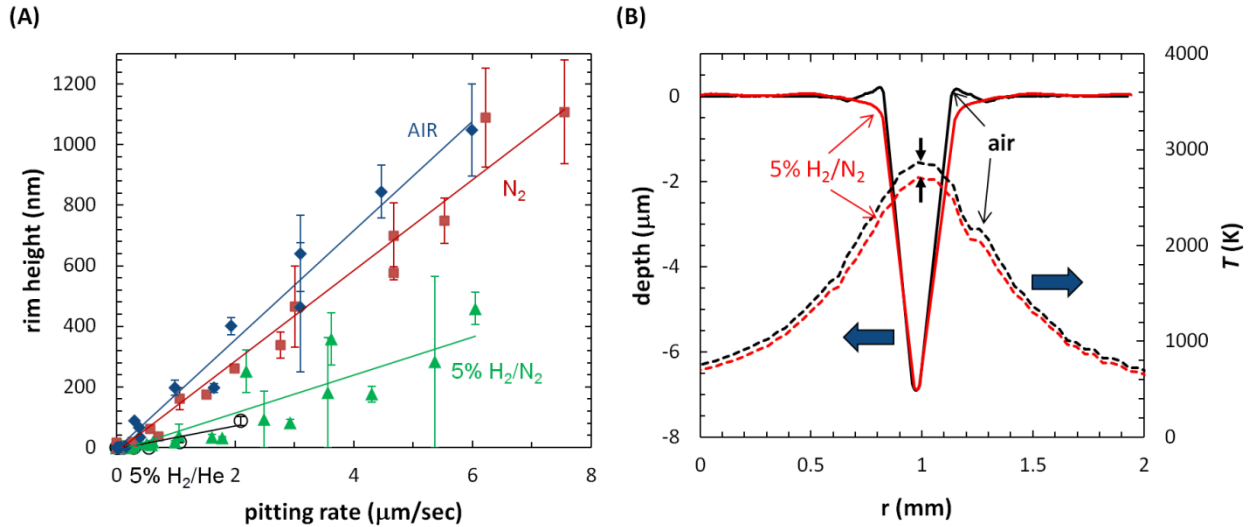


Fig. 3 (A) Comparison of the measured rim heights produced at the given pitting rate for the gases indicated. Rims and pit depths are measured after laser heating. (B) The thermal dependence of the gas-induced rim profiles is illustrated by the two pit spatial profiles produced in air and the reactive 5% H_2/N_2 gas. The pits have the same pit depths but different peak temperatures indicated by the arrows.

The observation that differences in rim height are thermally driven for steady heating is further demonstrated in Fig. 4. The temperature dependence of the pit volumes formed (Fig. 4(A)) for a fixed

exposure of 5 sec is shown with the corresponding rim height data (Fig. 4(B)). For the temperature regime where evaporation dominates pit shape, the amount of material removed is strongly dependent on the gas used and increases with application of air, 100% N₂, 5% H₂/N₂, and 5% H₂/He in that order for reasons already noted in section 3. 3, and consistent with previous measurements using a larger beam size of ≈ 1 mm [4]. However, in contrast with the apparent gas related differences in Fig. 3(A) when the rim data was given as a function of pitting rate, the data points for all gases collapsed on a single line when plotted over $1/T$. Thus demonstrating that rim formation in the near steady heating regime is a thermally activated process mostly independent of any solid-gas phase chemistry. The fitted activation energy closely matches that measured for the Corning 7980 glass used in this study, which can thus be attributed to the activation energy for viscous flow of silica [18]. At lower temperatures, evaporation, melting, and densification all play a role in determining final surface. Pit volume differences persist but with a weaker dependence on temperature than in the evaporation dominated regime, which mostly reflects the equilibrium constant and reaction free energy dependence on temperature [4]. At still lower temperatures below melting around 1800K down to 1450K, the shape of the pit is dominated by silica densification since both evaporation and flow become negligible at these temperatures and over the 5 sec exposure time scale. Under these low temperature conditions gas chemistry seems to have limited effect on pit volume as expected since most of the pitting would occur through structural relaxation rather than chemical reactivity. The three processes affecting pit shape are illustrated in the Fig. 4(C) spatial profiles that clearly show the combined effect of densification and evaporation at the intermediate temperature (red curve), the less complex shape of the densified region with a depth of 0.05 μm at the lowest temperature (orange curve), and the evaporation pit (depth = 1.85 μm) at the highest temperature with the rim protruding from melting and flow (black curve). The rimless pits mostly occur for heating conditions where evaporation is minimal. However, a more reactive gas should enable practical etching rates while avoiding rim formation, in particular for a material like fused silica with a very high softening temperature ($T_g = 1853\text{K}$ for Corning 7980). The transition points for the creation of rimless pits occurs around T_g as expected in the 1820K-2000K temperature range, and appears to be gas dependent, with air being the first in the series to reach the rimless regime, followed closely by 5% H₂/ He, 100% N₂, and 5% H₂/N₂ (Fig. 4B). The reason for this apparent gas specific shift in T_g is not clear, but for the purpose of producing rimless laser-etched features at the sub-nanometer scale, air and 5% H₂/He are most effective, with 5% H₂/He having the advantage of higher etch rates.

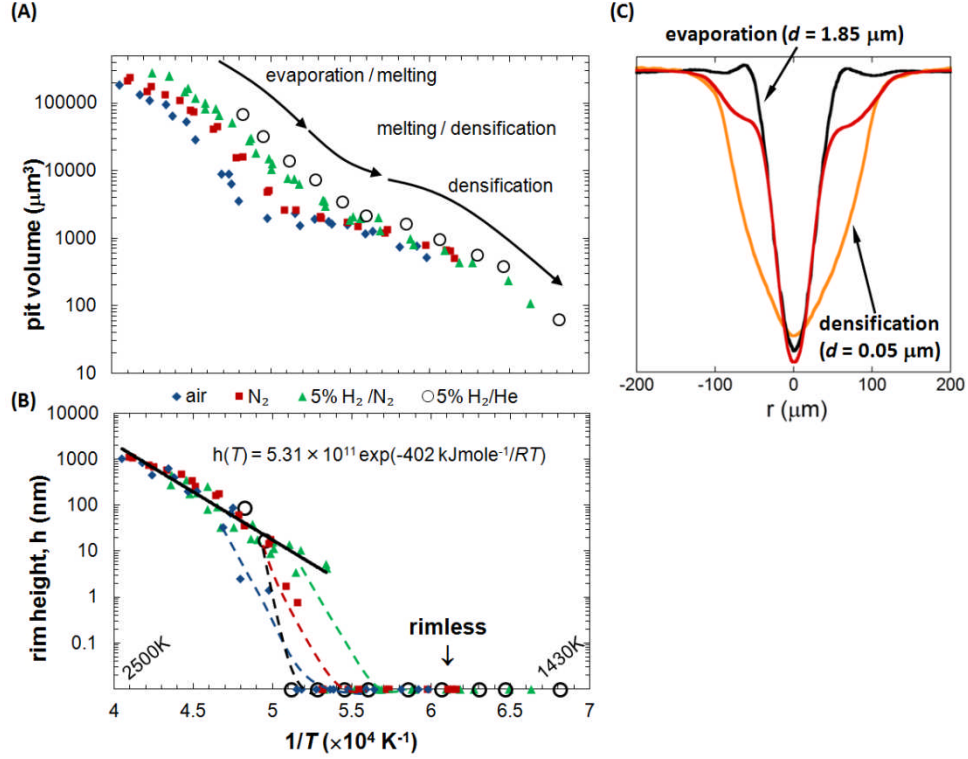


Fig. 4 (A) Experimental pit volume and (B) rim height dependence on temperature and gas, with regions for the three surface shaping processes (evaporation, melting/flow, and densification) delineated with the segmented arrows. The Arrhenius least square fit of the rim height data is shown (black line), with the value for viscous flow activation energy included ($E_a = 402 \text{ kJ/mole}$). (C) Spatial profile measurements illustrating the three surface shaping processes using the following conditions. Black curve, “evaporation” $T = 2110\text{K}$, with pit depth of $1.85 \mu\text{m}$ and the rim produced by melting and flow. Red curve, combined evaporation and densification $T = 1940\text{K}$, with pit depth of $0.242 \mu\text{m}$. Orange curve “densification” $T = 1770\text{K}$, with pit depth of $0.053 \mu\text{m}$. All laser exposures were fixed at 5 sec for the data shown in (A), (B), and (C), with fixed beam diameter of $400 \mu\text{m}$ ($1/e^2$).

4 Conclusions

Pitting rates and surface shape of CO_2 laser heated fused silica were measured for oxidizing, reducing, and neutral gas flow conditions over a range of dynamic and steady laser heating times from $10 \mu\text{s}$ up to 5 sec. Reducing atmosphere produced the greatest etch rates, while minimizing rim size, followed by neutral and oxidizing atmospheres. The temperature and etch rate dependence of rim formation reveal that the surface tension driven viscous flow process is mostly thermally activated for steady heating, with some possible added effect of gas reactivity-chemicapillarity apparent in the H_2 exposure for the dynamic (short pulse) heating experiments. Over the range of laser exposure and power used, the rim height exhibited a complex fluctuating behavior, although H_2 treatment produced systematically lower rims, even for $< 100 \text{ ms}$ pulse length where H_2 had no apparent effect on etch rates. The interplay of the fundamental temperature dependent material properties, coupled to the reactive surface environment still have to be determined for a quantitative description of the differences in gas-induced rim formation, especially under dynamic thermal loading. This study suggests however that with highly reactive gas phase conditions, rimless etch pits or machined features can be produced under steady and

unsteady heating. The only limitation being the mass transport rate of the reactants relative to that of the decomposition reaction for practical laser-based etching. The resulting more planar surface should reduce beam modulation and damage in optical materials used for high power laser application. In general, the reactive gas approach would benefit applications where sub-nanometer “rimless” laser-induced features are required.

Acknowledgments This work performed under the auspices of the U.S. Department of Energy by Lawrence Livermore National Laboratory under Contract No. DE-AC52-07NA27344.

References

- 1 T. A. Laurence, J. D. Bude, S. Ly et al., Optics Express **20**, 11561 (2012).
- 2 I. L. Bass, V. G. Draggoo, G. M. Guss et al., High-Power Laser Ablation VI, Pts 1 and 2 **6261**, A2612 (2006); I. L. Bass, G. M. Guss, M. J. Nostrand et al., presented at the Laser-Induced Damage in Optical Materials: 2010, Boulder, CO, USA, 2010 (unpublished).
- 3 A. F. H. Kaplan, Journal of Applied Physics **79**, 2198 (1996).
- 4 S. Elhadj, M. J. Matthews, S. T. Yang et al., Optics Express **20**, 1575 (2012).
- 5 H. L. Schick, Chemical Reviews **60**, 331 (1960).
- 6 M. J. Matthews, I. L. Bass, G. M. Guss et al., presented at the Laser-Induced Damage in Optical Materials: 2007, Boulder, CO, USA, 2007 (unpublished).
- 7 W. D. Kingery, Journal of the American Ceramic Society **42**, 6 (1959); N. M. Parikh, Journal of the American Ceramic Society **41**, 18 (1958).
- 8 S. C. Chen, D. G. Cahill, and C. P. Grigoropoulos, Journal of Heat Transfer-Transactions of the Asme **122**, 107 (2000); T. J. Mcneil, R. Cole, and R. S. Subramanian, Journal of the American Ceramic Society **68**, 254 (1985).
- 9 N. Shen, M. J. Matthews, J. E. Fair et al., Applied Surface Science **256**, 4031 (2010).
- 10 R. Bruckner, JOURNAL OF NON-CRYSTALLINE SOLIDS **5**, 123 (1970); R. Brückner, Journal of Non-Crystalline Solids **5**, 123 (1970); J. E. Shelby, JOURNAL OF NON-CRYSTALLINE SOLIDS **349**, 331 (2004).
- 11 R. H. Doremus, Journal of Applied Physics **92**, 7619 (2002).
- 12 S. T. Yang, M. J. Matthews, S. Elhadj et al., Journal of Applied Physics **106**, 103106 (2009).
- 13 S. Elhadj, M. J. Matthews, Steven T. Yang et al., presented at the Laser-Induced Damage in Optical Materials: 2009 Proceedings, Boulder, CO, 2009, 2009 (unpublished).
- 14 S. Elhadj, M. J. Matthews, S. T. Yang et al., Applied Physics Letters **96**, 071110 (2010).
- 15 S. Elhadj, S. R. Qiu, A. M. Monterrosa et al., Journal of Applied Physics **111** (2012).
- 16 J. E. Shelby, Journal of Applied Physics **51**, 2589 (1980).
- 17 G. A. Parks, Journal of Geophysical Research **89**, 3997 (1984).
- 18 V. Zandian, J. S. Florry, and D. Taylor, British Ceramic Transactions and Journal **90**, 59 (1991).
- 19 V. Lou, R. Sato, and M. Tomozawa, Journal of Non-Crystalline Solids **315**, 13 (2003).